

Article

Analyzing Performances of Different Atmospheric Correction Techniques for Landsat 8: Application for Coastal Remote Sensing

Christopher O. Ilori ^{1,*}, Nima Pahlevan ^{2,3}  and Anders Knudby ⁴ ¹ Simon Fraser University, 8888 University Drive, Burnaby, BC V5A 1S6, Canada² NASA Goddard Space Flight Center, 8800 Greenbelt Road, Greenbelt, MD 20771, USA; nima.pahlevan@nasa.gov³ Science Systems and Applications, Inc., 10210 Greenbelt Road, Suite 600 Lanham, MD 20706, USA⁴ University of Ottawa, 60 University Private, Ottawa, ON K1N 6N5, Canada; aknudby@uottawa.ca

* Correspondence: cilori@sfsu.ca; Tel.: +1-778-929-5350

Received: 28 January 2019; Accepted: 18 February 2019; Published: 25 February 2019



Abstract: Ocean colour (OC) remote sensing is important for monitoring marine ecosystems. However, inverting the OC signal from the top-of-atmosphere (TOA) radiance measured by satellite sensors remains a challenge as the retrieval accuracy is highly dependent on the performance of the atmospheric correction as well as sensor calibration. In this study, the performances of four atmospheric correction (AC) algorithms, the Atmospheric and Radiometric Correction of Satellite Imagery (ARCSI), Atmospheric Correction for OLI ‘lite’ (ACOLITE), Landsat 8 Surface Reflectance (LSR) Climate Data Record (Landsat CDR), herein referred to as LaSRC (Landsat 8 Surface Reflectance Code), and the Sea-Viewing Wide Field-of-View Sensor (SeaWiFS) Data Analysis System (SeaDAS), implemented for Landsat 8 Operational Land Imager (OLI) data, were evaluated. The OLI-derived remote sensing reflectance (R_{rs}) products (also known as Level-2 products) were tested against near-simultaneous in-situ data acquired from the OC component of the Aerosol Robotic Network (AERONET-OC). Analyses of the match-ups revealed that generic atmospheric correction methods (i.e., ARCSI and LaSRC), which perform reasonably well over land, provide inaccurate Level-2 products over coastal waters, in particular, in the blue bands. Between water-specific AC methods (i.e., SeaDAS and ACOLITE), SeaDAS was found to perform better over complex waters with root-mean-square error (RMSE) varying from 0.0013 to 0.0005 sr^{-1} for the 443 and 655 nm channels, respectively. An assessment of the effects of dominant environmental variables revealed AC retrieval errors were influenced by the solar zenith angle and wind speed for ACOLITE and SeaDAS in the 443 and 482 nm channels. Recognizing that the AERONET-OC sites are not representative of inland waters, extensive research and analyses are required to further evaluate the performance of various AC methods for high-resolution imagers like Landsat 8 and Sentinel-2 under a broad range of aquatic/atmospheric conditions.

Keywords: atmospheric correction; remote sensing reflectance; Landsat 8; band adjustment; validation; AERONET-OC

1. Introduction

Ocean colour (OC) remote sensing provides information on in-water optical properties indicating the concentrations of water constituents such as chlorophyll-a. In optically shallow waters, depth and seafloor spectral reflectance may also be estimated using remotely sensed images. Information about near-surface, in-water optical properties, in the form of water quality maps, can provide advance warning of algal bloom development [1] and potentially lead to early mitigation efforts to reduce

health risks and financial losses. Bathymetric maps, derived from water depth estimates, can be used to produce or update navigational charts [2], reducing the risk of ship groundings. Benthic habitat maps, inferred from seafloor spectral reflectance, can be used to track changes in the distribution of seafloor habitats [3,4]. However, extracting ocean colour products such as chlorophyll-a, water depth, and bottom types from remotely sensed images is difficult because, over blue ocean waters, only ~10% of the total signal that reaches the TOA (Top of Atmosphere) typically comes from within the water column [5]. In addition to the radiation leaving the water column (L_w), the TOA radiance measured by satellite sensors includes contributions from scattering and absorption in the atmosphere and reflection at the sea surface [6]. It is important to estimate and account for the contribution from these other sources in order to estimate L_w , which is readily normalized by the total downwelling irradiance just above the sea surface to yield the remote sensing reflectance (R_{rs}).

Atmospheric effects are removed through atmospheric correction (AC) [7], but residual errors in AC can introduce large uncertainties in R_{rs} estimates, resulting in erroneous retrieval of OC products such as apparent optical properties [8]. In open ocean waters, where phytoplankton governs the optical regime, it can be conveniently assumed that there is no water-leaving radiance in the near-infrared (NIR) region, such that any measured TOA radiance in this spectral band is attributed to atmospheric path radiance and reflectance from the water surface. While this assumption is valid for open-ocean waters, in shallow or optically complex waters that are, in general, characterized by a combination of constituents, such as phytoplankton, coloured dissolved organic matters, and suspended particulate matters, $R_{rs}(\text{NIR})$ may be significantly greater than zero because of bottom reflectance (which can come from highly reflective near-surface vegetation such as kelp and seagrasses) and backscattering by suspended materials [9]. This can lead to over-correction of atmospheric and surface reflectance effects, leading to underestimation and even negative L_w estimates within the shorter wavelengths used to derive OC products [9,10]. To account for the non-negligible $R_{rs}(\text{NIR})$, algorithms that work for Case 2 waters have been developed (e.g., [10–12]) and tested (e.g., [13,14]). With these efforts, it is now possible to retrieve L_w over coastal waters. However, the low spatial resolution of traditional ocean colour sensors inhibits the detection of detailed features that are not easily discernible in coarse-resolution satellite images. The recent availability of higher-resolution satellite sensors, e.g., Landsat 8 Operational Land Imager (OLI) and Sentinel-2 Multispectral Instrument (MSI), with adequate spectral and radiometric characteristics for ocean colour applications, has the potential to greatly improve coastal ocean colour applications, including water quality [15,16], bathymetry, and seafloor habitat mapping [17].

Optimizing the utility of the OLI sensor for aquatic science and applications requires validating R_{rs} products to better understand their potential and limitations. A few recent studies have started investigating the quality of OLI-derived R_{rs} for coastal applications. For example, Pahlevan et al. [15] used the AC scheme in SeaDAS software package to determine the best Landsat 8 band combinations that can minimize error in R_{rs} retrieval over different coastal water types at select AERONET-Ocean Colour (OC) sites. Using newly computed calibration gains, they revealed that OLI-derived R_{rs} estimates are as good as those from other ocean colour sensors. Likewise, the work of Franz et al. (2015) [18] illustrated the potential of OLI data for water-related studies. By employing the AC process in the SeaDAS Level-2 processing algorithm (l2gen), they assessed the quality of OLI-derived R_{rs} and subsequently retrieved the chlorophyll-a concentration over the Chesapeake Bay, USA. In agreement with Pahlevan et al. (2017a) [15], they found that with a precise AC procedure, the high radiometric quality and improved imaging capabilities of OLI hold great promise for satellite-based coastal monitoring. Doxani et al. (2018) [19] tested a wide range of AC algorithms over different land cover types, highlighting the strengths and limitations of each algorithm. More recently, Wei et al. (2018) [20] also assessed four AC algorithms with a focus over water bodies, revealing that the NIR-short-wave infrared (SWIR) approach implemented in SeaDAS produced the most robust R_{rs} estimates from Landsat 8. However, none of these studies examined the effects of environmental variables on the R_{rs} retrieval accuracy of different AC algorithms.

With the increase in usage of OC products among the science community, and the need for robust R_{rs} products, it is important to understand the potential of AC algorithms. Most of the ocean colour community has for years been using water-based AC methods for a wide range of applications from coastal to inland waters, so it is important that the effects of relevant environmental variables on the R_{rs} retrieval accuracy of these AC algorithms is examined. Such knowledge may assist in the choice of AC algorithm for a given set of environmental conditions, and/or improved R_{rs} retrieval under a wider range of conditions. Equally important is that other users interested in studying inland waters (e.g., biogeochemists, aquatic biologists) fully understand the accuracy of generic AC processors, in particular the land surface reflectance product, which is commonly used.

Here, we pursued an approach similar to Pahlevan et al. (2017a) [15], but expanded it by evaluating the performances of four different AC algorithms to determine which method produces the most robust R_{rs} products in shallow coastal waters. Also, like Doxani et al. (2018) [19], we tested both land-based and water-based algorithms at multiple sites, but covered more sites over a longer time period to better capture space-time dynamics related to water optical properties. Using 54 in-situ measurements from 14 AERONET-OC sites, we (1) tested the following algorithms for atmospheric correction of Landsat 8 images: (a) Atmospheric and Radiometric Correction of Satellite Imagery (ARCSI) [21], (b) the Atmospheric Correction for OLI ‘lite’ (ACOLITE) [22], (c) SeaDAS [8], and (d) the United States Geological Survey’s standard land-based AC used to produce the Landsat 8 Surface Reflectance (LSR) Climate Data Record (Landsat CDR), herein referred to as LaSRC [23]; (2) analysed the differences in spectral bands between satellite and in-situ measurements; and (3) examined the effects of three key environmental variables on the R_{rs} retrieval accuracy of water-based AC algorithms. To our knowledge, this is the first inter-comparison exercise that tested AC algorithms using representative data from many coastal sites with varying atmospheric conditions and optical properties, combining the three approaches mentioned above in a single study.

2. Materials and Methods

2.1. Landsat 8 OLI Data

OLI measures TOA radiance in the visible, NIR, and short-wave infrared (SWIR) bands, at a spatial resolution of 30 m. Compared to its predecessors, OLI includes a new coastal/aerosol band (435–451 nm) in addition to the traditional blue (452–512 nm), green (533–590 nm), and red (636–673 nm) bands. The addition of a new band, together with enhanced spectral coverage and radiometric resolution, enables improved observation of water bodies from space and the ability to estimate the concentration of atmospheric aerosols for AC [16,24,25] (note that aerosol estimation for AC by the coastal band is done over land). Compared to data from existing global ocean colour missions, the higher spatial resolution has the potential to make important contributions to ocean colour remote sensing, such as separating and mapping in-water constituents in coastal waters [16,25]. Although OLI signal-to-noise ratios (SNRs) (Table 1) are generally lower than those of heritage ocean colour sensors such as SeaWiFS or the Moderate Resolution Imaging Spectroradiometer onboard Aqua (MODISA), its enhanced SNR across all bands compared to the past Landsat missions improves OLI’s ability to measure subtle variability in near-surface conditions and ultimately make OLI products a valuable source of data for ocean colour studies [16,18].

Table 1. Comparison of the band centres and the signal-to-noise ratios of MODIS and Landsat 8 Operational Land Imager (OLI) at specified levels of typical spectral radiance.

	Band centres (nm)						
MODIS	443	488	555	645	858	1640	2130
SeaWiFS	443	490	555	670	865	NA	NA
OLI	443	482	56	655	865	1609	2201

Table 1. Cont.

Signal-to-noise ratio (SNR)							
MODIS	838	802	228	128	201	275	110
SeaWiFS	950	1000	850	500	350	NA	NA
OLI	344	478	279	144	67	30	14
L_{typ} ($\text{W m}^{-2} \mu\text{-}1 \text{sr}^{-1}$)							
MODIS	4.9	32.1	29	21.8	24.7	7.3	1.0
SeaWiFS	70.2	53.1	33.9	8.3	4.5	NA	NA
OLI	69.8	55.3	27.5	13.4	4.06	0.353	0.0467

2.2. AERONET-OC Data

To validate the performance of the AC processors applied to the OLI data, we acquired 122 cloud-screened and fully quality-controlled Level 2.0 AERONET-OC in-situ measurements of normalized water-leaving radiance (nL_w) for 14 AERONET-OC sites, including 12 coastal sites (i.e., Galata Platform, Gloria, GOT Seaprism, Gustav Dalen Tower, Helsinki Lighthouse, Long Island Sound Coastal Observatory (LISCO), Martha's Vineyard Coastal Observatory (MVCO), Thornton C-Power, USC Seaprism, Venise, WaveCIS Site CSI-6, Zeebrugge-MOW1) and two lake sites (Lake Erie, Palgrunden) (Figure 1). AERONET-OC, managed by NASA's Goddard Space Flight Center (GSFC) [26], is a sub-network of the AERONET federated instrument [27,28]. Although OLI and AERONET-OC have somewhat different spectral bands, a set of comparable bands centred at 441 nm, 491 nm, 551 nm, and 667 nm can be used for cross-comparison purposes. Thus, AERONET-OC data were collected in four spectral bands centred at 441, 491, 551, and 667 nm, for comparison with OLI's four visible bands, centred at 443, 483, 561 and 655 nm. Note that there is a slight difference, i.e., ± 1 to ± 3 nm, in all four bands among measurements at different sites. As R_{rs} is not directly available from the AERONET-OC sites, the normalized water-leaving radiances (nL_w , $\text{W m}^{-2} \text{sr}^{-1}$) were divided by the top-of-the atmosphere (TOA) solar irradiance (F_0) [29] to obtain R_{rs} .

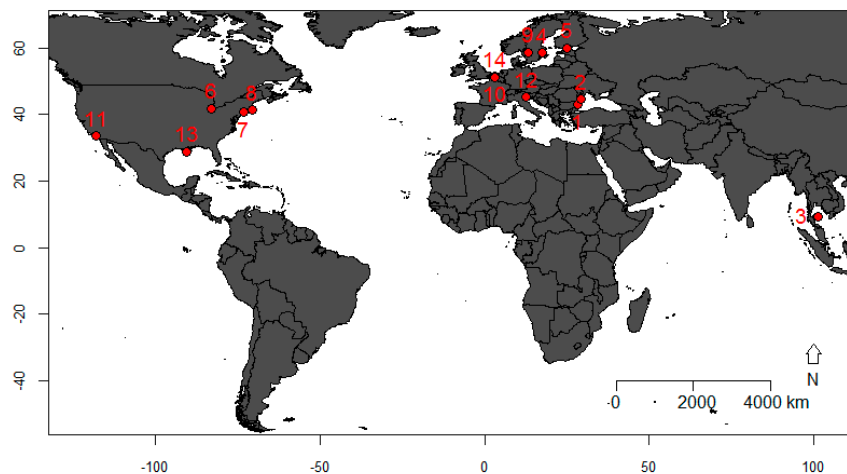


Figure 1. Map showing the 14 validation sites from the ocean colour (OC) component of the Aerosol Robotic Network (AERONET-OC) station. 1: Galata, 2: Gloria, 3: GOT Seaprism, 4: Gustav Dalen Tower, 5: Helsinki, 6: Lake Erie, 7: Long Island Sound Coastal Observatory (LISCO), 8: Martha's Vineyard Coastal Observatory (MVCO), 9: Palgrunden, 10: Thornton C-Power; 11: USC Seaprism, 12: Venise, 13: WaveCIS Site CSI-6, 14: Zeebrugge-MOW1.

2.3. Match-Up Exercise

To obtain the in-situ R_{rs} data needed to test AC procedures for OLI, we performed a match-up exercise between the AERONET-OC measurements and OLI data as follows: (i) Using the OLI metadata

database file provided by the United States Geological Survey (USGS), python code was created to automatically retrieve all Landsat 8 OLI scenes and the contemporaneous AERONET-OC data (from the AERONET-OC website) that were within a ± 30 -min time window of Landsat 8 overpass times, for the April 2013 to May 2017 timeframe (note that a strict time window of ± 30 min, which reduces the number of match-up pairs, was used to limit the error introduced by water movement between satellite and AERONET-OC observations, and ensure the quality of match-ups). This yielded a text file containing a total of 122 match-ups with coincident satellite and in-situ data for 14 AERONET-OC sites (Figure 2), as well as information on aerosol optical thickness, solar zenith angles (SZA), and wind speed for each match-up. All corresponding OLI scenes were subsequently bulk-downloaded using Landsat-util, a tool to automatically find and download multiple Landsat 8 scenes. Some of the 122 OLI scenes visibly contained a non-negligible amount of specular reflection off the sea surface (sunglint) in the area of the AERONET-OC site. As not all AC algorithms have the capacity for sunglint correction, to obtain realistic and comparable R_{rs} across all AC methods, scenes with visible specular reflection were excluded, leaving 69 of the original 122 scenes; (ii) Following the approach of Bailey and Werdell (2006) [30], a regional subset of Landsat 8 data was generated for each scene by (1) extracting a 7×7 pixel window centred on the location of the AERONET-OC site, and (2) removing the centre 3×3 pixels from that window to limit the effect of noise from the site's superstructures and shadows cast by it; (iii) For SeaDAS, remaining low-quality pixels were then removed by employing the internal SeaDAS exclusion flags, which include flags for land, clouds, cloud-shadow, ice, stray light, low nL_w (555), high viewing zenith angle ($>60^\circ$), high sunglint, and high TOA radiance. Scenes without any unflagged pixels were eliminated from the match-up exercise, leaving 54 scenes for comparison with AERONET-OC data. Similarly, internal ACOLITE exclusion flags were used to remove low-quality pixels for ACOLITE, which left 56 scenes for AERONET-OC comparison. The 54 scenes remaining after applying the SeaDAS exclusion flags also passed ACOLITE's exclusion flags, and were therefore used for further analysis. To ensure an unbiased inter-comparison, we included pixels with negative (Table A3) and zero R_{rs} retrievals from all methods; (iv) We then obtained the per-band median R_{rs} values of the unflagged pixels from each Landsat regional subset for final comparison with in-situ data, and used the median AERONET-OC measurements collected within the ± 30 -min window of the Landsat 8 overpass to represent in-situ match-ups.

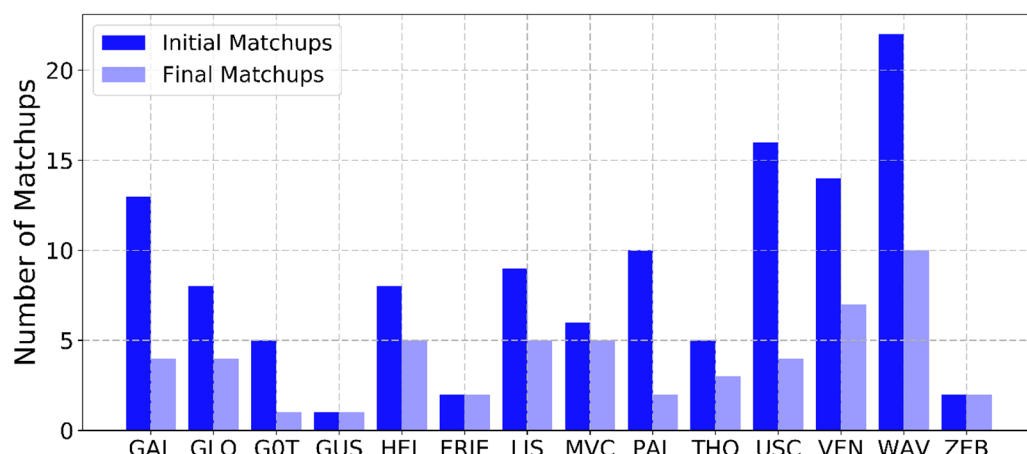


Figure 2. Number of match-ups between Landsat 8 OLI scenes and AERONET-OC site measurements within ± 30 -min window of the Landsat 8 overpass (GAL: Galata, GLO: Gloria, GOT: Got Seaprism, GUS: Gustav Dalen Tower, HEL: Helsinki, ERIE: Lake Erie, LIS: LISCO, MVC: MVCO, PAL: Palgrunden, THO: Thornton C-Power, USC: USC Seaprism, VEN: Venise, WAV: WaveCIS Site CSI-6, ZEB: Zeebrugge-MOW1). Dark blue represents the total number of initial match-ups within a ± 30 -min time window of the Landsat 8 overpass times for each site. Light blue represents the total number of final match-ups used for analysis after excluding scenes with sunglint and performing the match-up exercise.

2.4. Data Processing

2.4.1. Description of Atmospheric Correction Algorithms

Atmospheric correction of the OLI data was carried out using four algorithms: ARCSI, ACOLITE (version 20170113.0), SeaDAS (version 7.4), and LaSRC. Note that LaSRC is a product that has already been processed for surface reflectance by the United States Geological Survey (USGS). Both ACOLITE and SeaDAS have been specifically designed for AC over water surfaces, whereas ARCSI and LaSRC have not; we therefore refer to the latter two as land-based methods. The output of the water-based methods is R_{rs} , which is directly comparable to the in-situ data from AERONET (after conversion: $R_{rs} = nL_w / F_0$), while the output of the land-based methods is in units of above-surface diffuse reflectance $R(0^+)$, which we converted to R_{rs} using:

$$R_{rs} = R(0^+) / \pi \quad (1)$$

ARCSI is an open-source software program developed at Aberystwyth University [21]. It is a relatively new AC algorithm with functionalities to process multispectral images from both commercial and publicly available sensors and also to obtain processed data for direct use in remote sensing analyses [31]. It is a command line tool where Py6S [32] can be implemented to correct multispectral images to above-surface diffuse reflectance using the 6S model [33], which simulates ground and atmospheric radiation under a variety of conditions. Within the 6S method, input parameters such as the Aerosol Optical Thickness (AOT), vertical column water vapour, and ozone concentration are automatically used by the 6S method to characterize the state of the atmosphere.

ACOLITE is a binary distribution of Landsat 8 OLI and Sentinel-2 MSI processing software developed by the Royal Belgian Institute of Natural Sciences [22,34]. It is an image-based AC algorithm that estimates L_w by correcting for molecular and aerosol scattering in the atmosphere using the Gordon and Wang (1994a) approach [5]. Molecular reflectance correction, based on viewing and illumination geometries, is performed with a 6SV-based look-up table [33]. Unlike SeaDAS, which uses 80 aerosol models for aerosol estimation [5,35], aerosol reflectance is estimated by determining aerosol types from the ratio of reflectances in two SWIR bands over water pixels where reflectance can be assumed zero, an approach similar to Ruddick et al. (2000) [36]. Based on this assumption, it also retrieves water-leaving reflectances in both the visible and NIR bands together with other parameters of interest in marine and inland waters. ACOLITE is primarily designed for processing Landsat 8 OLI data for aquatic remote sensing applications, but has recently been modified and updated to include processing of Sentinel-2 MSI data [37].

LaSRC is a Level-2 data set produced and released as a provisional product by the USGS since January 2015, primarily to support terrestrial remote sensing applications. Unlike the precursor algorithm, i.e., Landsat Ecosystem Disturbance Adaptive Processing System (LEDAPS), used for previous Landsat satellites such as Landsat 4-5 Thematic Mapper (TM) and Landsat 7 Enhanced Thematic Mapper Plus (ETM+), which used the 6S model, LaSRC is generated using a dedicated Landsat Surface Reflectance code [24]. Data are available as standalone climate data records (CDRs) that represent specific geophysical and biophysical properties of the land surface [23]. AC is mainly based on the MODIS collection 6-AC algorithm, which uses a radiative transfer model for the inversion of atmospheric parameters such as aerosol and water vapour [24]. It should be noted that surface reflectance is provided in seven spectral bands (the first seven OLI bands) only for scenes with a solar zenith angle less than 76° , and that the 443 nm and 482 nm bands are not suitable for analysis as they are ‘consumed’ for aerosol inversion tests within the LaSRC. Although still provisional and under continuous improvement, LaSRC has been validated and assessed for land applications [38–41], and has a dedicated aerosol retrieval algorithm for pixels over water [23].

SeaDAS, which uses an NIR and a SWIR band for aerosol estimation for processing OLI imagery, contains an AC scheme originally designed for open ocean water based on the assumption of negligible

L_w in the NIR bands. This approach, which is NASA's operational AC algorithm [5], includes an l2gen (Level 2 generator) to retrieve R_{rs} and other optical and geophysical water and atmospheric properties. Following some improvements to estimation of aerosol contributions (e.g., [12,42,43]) the l2gen processor in SeaDAS can now be used for deriving R_{rs} in moderately turbid coastal waters [14].

2.4.2. Atmospheric Correction Procedure and Validation

To derive R_{rs} , all four AC algorithms were parameterized using their default processing options. In addition, the following processing was implemented: (1) In SeaDAS, out-of-band correction options were set to zero (outband_opt = 0), i.e. R_{rs} was reported at full bandpass, without correction to the nominal band centre, and no sunglint correction was implemented (glint_opt = 0) since there was no such correction option available for other algorithms; (2) In ARCSI, the 'clear water' option was used for the reflectance of a ground target as processing requires an option from 'green vegetation', 'clear water', 'sand', or 'lake water'. Also, AOT and other atmospheric parameters were automatically identified and estimated by ARCSI during batch processing. To derive AOT for each scene, realistic minimum and maximum values of 0.001 and 0.9, respectively, were manually specified; (3) Finally, to allow for consistency among all methods, we assumed a perfect sensor calibration by applying unity gains for vicarious calibration across all bands for all processors. For SeaDAS, aerosol correction was implemented following the Gordon and Wang (1994a) approach [5], with the NIR/SWIR correction option (865–1609 nm band combination) as suggested in Pahlevan et al. (2017a) [15] and Mobley et al. (2016) [7]. ACOLITE aerosol correction was implemented using the default SWIR option (1609 and 2201 nm band combination) which computes Rayleigh-corrected reflectance from the SWIR bands for moderate and turbid waters. Each AC algorithm was applied to the final 54 Landsat 8 OLI scenes, representing a wide variety of coastal and atmospheric conditions (Table A1). When comparing their performance, we considered AERONET-OC data as the reference with negligible uncertainties. Note that uncertainties in the AERONET-OC in-situ measurements are ~5% in the blue to green bands and ~8% in the red band [26]. As noted in Pahlevan et al. (2017b) [44] and Mélin and Sclep (2015) [45], compensating for discrepancies arising from the differences in nominal band centre wavelengths is crucial for obtaining a robust match-up analysis across all spectral bands (in particular for OLI's relatively broad spectral bands). To this end, we carried out a spectral band adjustment using the deep neural network approach as described in Pahlevan et al. (2017b) [44] and compared R_{rs} derived with and without band adjustments.

The algorithm performance was compared using six metrics including:

$$\text{Root-Mean-Square Error (RMSE)} = \sqrt{\frac{1}{n} \sum_{i=1}^n (x^{mea} - x^{est})^2} \quad (2)$$

$$\text{mean bias} = \frac{\sum_{i=1}^n (x^{mea} - x^{est})}{n} \quad (3)$$

$$\text{Spectral Angle} = \cos^{-1} \left(\frac{\sum_{i=1}^n x^{mea} \cdot x^{est}}{\sqrt{\sum_{i=1}^n x^{mea^2}} \sqrt{\sum_{i=1}^n x^{est^2}}} \right) \quad (4)$$

as well as the coefficient of determination (R^2), slope, and intercept of the line fitted using least-squares regression between in-situ and satellite R_{rs} estimates. The x^{mea} and x^{est} are AERONET-OC and satellite-derived R_{rs} data, respectively. The Spectral Angle (SA), which is insensitive to spectral amplitude, is used to quantify the similarity between satellite and in-situ R_{rs} spectra. Values close to 0 indicate high similarity.

3. Results and Discussion

3.1. Validation of AC Algorithms

Scatter plots showing the estimated (OLI) and observed (AERONET-OC) R_{rs} values for each match-up are presented in Figure 3, and summary statistics are tabulated in Table 2. There are clear differences between the water-based and land-based AC algorithms, with SeaDAS and ACOLITE outperforming ARCSI and LaSRC in all metrics for all bands, with only one exception (slope for $R_{rs}(482)$). Between the two water-based methods, SeaDAS outperforms ACOLITE in every metric for all bands, with the exception of slopes for $R_{rs}(482)$, $R_{rs}(561)$, and $R_{rs}(655)$. SeaDAS had RMSEs close to zero between 0.0013 and 0.0005 1/sr across all four wavelengths demonstrating a high degree of similarity between in-situ and OLI-estimated R_{rs} with OLI data processed through SeaDAS (Table 2). A comparison of RMSE results of the per-band difference with and without band adjustments (Figure A1) shows that SeaDAS was the AC method most sensitive to spectral band differences, with the largest improvement of band adjustment occurring in the 655 nm channel. Spectral Angle values obtained for all algorithms showed that SeaDAS and ACOLITE have the highest similarity with in-situ R_{rs} spectra (ARCSI: 0.46, ACOLITE: 0.27, LaSRC: 0.53 and SeaDAS: 0.20).

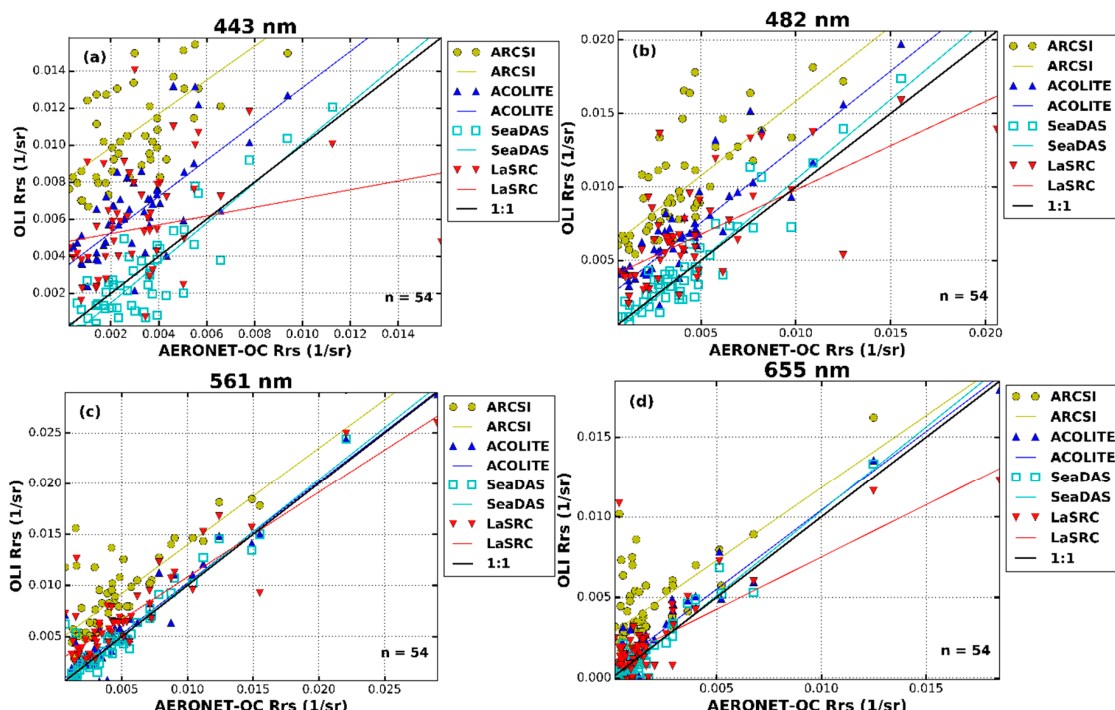


Figure 3. Scatterplots of the relationship between in-situ measurements (x-axis) and OLI estimates (y-axis) for each OLI band acquired over 14 AERONET-OC sites. Regression lines are shown in colours, while the thick dotted black lines are 1:1 lines. (a) 443 nm; (b) 482 nm; (c) 561 nm; (d) 651 nm.

The overall performance of SeaDAS reveals that the NIR-SWIR aerosol correction option can yield satisfactory results in low-to-moderately turbid waters. A possible reason for this is that the aerosol correction scheme, constructed following Ahmad et al. (2010) [42], was based on aerosol data obtained mainly from AERONET-OC sites [46]. Comparison of R^2 values among all methods shows that the lowest and most diverse values are in the 443 nm wavelength, with values between 0.05 and 0.84. For LaSRC in particular, the regression line for the comparison in the 443 nm wavelength deviates very much from the 1:1 line, yielding a poor R^2 and slope (Figure 3). The poor correlation and low RMSE (R^2 : 0.05, slope: 0.23) are mostly a result of the large discrepancies between the observed and estimated R_{rs} for the Zeebrugge-MOW1 site, where mean R_{rs} was underestimated by ~70%. This is the largest underestimation by any method, across all sites. For this site, which is one of the most turbid sites in

the AERONET-OC network, mean observed in-situ R_{rs} in the red band is 0.0155 sr^{-1} , making it the only site with $R_{rs}(655)$ one order of magnitude greater than the mean value of $\sim 0.001 \text{ sr}^{-1}$ observed for all 14 AERONET-OC sites. This level of turbidity is common for this site, which is located only $\sim 3.65 \text{ km}$ from the coastline and receives sediment-rich water inputs from nearby rivers, as also noted by Vanhellemont and Ruddick (2015) [47] and was clearly visible in additional scenes excluded during the match-up exercise. Note that the TOA radiance data were used ‘as is’ without optimizing the vicarious calibration gains (as computed by Pahlevan et al. (2017a) [15]), which might further improve R_{rs} retrievals. Similarly, none of the AC methods with different configuration capabilities that might improve performance were optimized as there was no optimal setting that would work for all cases considered in this paper.

Table 2. Statistical results for the retrieved remote sensing reflectance (R_{rs}) obtained for all processors with and without band adjustment (values in parenthesis represent results without band adjustment). Best metrics are highlighted in bold letters. After-band-adjustment linear fit, which was employed to reveal the relationship between in-situ and modelled R_{rs} , improves with increasing wavelength for both Atmospheric Correction (ACOLITE and SeaDAS), with R^2 values of 0.70/0.84, 0.85/0.92, 0.92/0.95, and 0.93/0.97 for bands 1 through 4 for ACOLITE/SeaDAS, respectively. A similar trend is seen for ARCSI and LaSRC, for the first three bands.

	R²	Slope	RMSE (1/sr)	Intercept	p-Values
<i>R_{rs} 443</i>					
ARCSI	0.43 (0.41)	0.91 (0.89)	0.0085 (0.0085)	0.0080 (0.0084)	8.92e-08
ACOLITE	0.70 (0.68)	0.97 (0.97)	0.0039 (0.0039)	0.0036 (0.0037)	4.16e-15
LaSRC	0.05 (0.05)	0.23 (0.25)	0.0042 (0.0042)	0.0050 (0.0050)	0.11
SeaDAS	0.84 (0.84)	1.08 (1.08)	0.0013 (0.0013)	-0.0006 (-0.0006)	2.36e-22
<i>R_{rs} 482</i>					
ARCSI	0.68 (0.63)	1.01 (0.92)	0.0065 (0.0063)	0.0060 (0.0061)	2.00e-13
ACOLITE	0.85 (0.79)	1.03 (0.94)	0.0032 (0.0031)	0.0027 (0.0029)	1.99e-14
LaSRC	0.44 (0.43)	0.60 (0.56)	0.0035 (0.0035)	0.0041 (0.0041)	3.77e-08
SeaDAS	0.92 (0.87)	1.09 (1.00)	0.0012 (0.0015)	-0.0002 (0.00009)	5.44e-30
<i>R_{rs} 561</i>					
ARCSI	0.77 (0.77)	0.95 (0.97)	0.0051 (0.0048)	0.0046 (0.0042)	5.27e-18
ACOLITE	0.92 (0.87)	1.00 (0.98)	0.0016 (0.0019)	0.0005 (0.0002)	1.38e-29
LaSRC	0.80 (0.78)	0.83 (0.83)	0.0030 (0.0029)	0.0027 (0.0025)	9.48e-20
SeaDAS	0.95 (0.92)	1.03 (1.21)	0.0012 (0.0011)	0.00005 (-0.0003)	1.13e-34
<i>R_{rs} 665</i>					
ARCSI	0.64 (0.63)	0.91 (1.06)	0.0033 (0.0034)	0.0028 (0.0026)	4.49e-13
ACOLITE	0.93 (0.89)	0.98 (1.13)	0.0010 (0.0013)	0.0006 (0.0005)	1.91e-31
LaSRC	0.52 (0.50)	0.65 (0.75)	0.0022 (0.0021)	0.0011 (0.0010)	8.39e-10
SeaDAS	0.97 (0.92)	1.01 (1.21)	0.0005 (0.0011)	-0.0001 (-0.0003)	4.00e-40

3.2. Inter-Comparison of Reflectance Spectra at Each Site

Comparison of mean estimated and observed R_{rs} at each AERONET-OC site (Figure A2) shows that all algorithms except SeaDAS generally overestimate R_{rs} across all wavelengths, with the largest and smallest overestimation occurring in the 443 and 665 nm wavelengths, respectively. This is further supported by the RMSE and bias results (Figure 4). The largest errors (RMSE) and overestimations (bias) are observed in the 443 nm wavelength, probably due to the strong atmospheric scattering in this band. ARCSI has the largest overall positive bias in this wavelength, and indeed the highest overestimation at each site. However, its R_{rs} results across all wavelengths at the Zeebrugge-MOW1 site compare well with R_{rs} estimates from SeaDAS and ACOLITE. This suggests that ARCSI has a low sensitivity to the high concentrations of suspended sediments that dominate this site, as reported by De Maerschalck and Vanlede (2013) [48]. This may also serve as an indication that ARCSI can better deal with turbid conditions than can LaSRC, which underestimated R_{rs} by $\sim 45\%$ at this site. The failure of LaSRC for this band is likely due to the fact that it is part of the bands used for the aerosol inversion scheme [23].

The best performance from LaSRC across all bands is at Lake Erie (with two match-ups) where all other AC algorithms except ARCSI also have the best match with in-situ R_{rs} . LaSRC outperforms other algorithms for the first three bands. Percentage difference values are 4.5%, −3.2%, and −0.3% for the first three bands, respectively. For ACOLITE and SeaDAS, the corresponding values are 28.8/−20.7%, 13.6/−12.8%, and −0.4/−6.4%. Indeed, at this site LaSRC has the best R_{rs} estimate of all methods in the 561 nm channel, while ACOLITE has the best R_{rs} estimate in the 655 nm channel, with a percentage difference of −1.3%, whereas SeaDAS and LaSRC are −18.2% and −30%, respectively. Similar to the estimated R_{rs} by LaSRC in Lake Erie in the 561 nm channel, LASRC-derived $R_{rs}(561)$ also agrees well with that of in-situ at Zeebrugge-MOW1 site; the percentage difference here is −0.25%. For SeaDAS and ACOLITE, these values are 6.7% and 4.1%, respectively. LaSRC also outperforms other AC algorithms in the 443, 482, and 655 nm channels at the GOT-Seaprism site, with only one match-up. Percentage differences between estimated and in-situ R_{rs} are 8.8%, 11.1%, and −40.8%, respectively. For ACOLITE and SeaDAS, the corresponding values are 87.7/−79.3%, 60.9/−46.3%, and 96.4/−127.6%. This is the only site where SeaDAS uncharacteristically underestimates R_{rs} across all four bands. While any conclusion is tentative as GOT Seaprism (2014-026) only has one match-up, the poor performance of SeaDAS here is as a result of algorithm failure (very low R_{rs} in 443, 482, and 561 nm wavelengths, and negative R_{rs} in 655 nm wavelength), which can be attributed to conditions such as residual effects from cloud shadow or overcorrection for aerosol contribution in one or more visible band. Overcorrection typically occurs when water-leaving radiance is non-negligible in the band used to estimate the aerosol contribution [49]. Other instances of failure (as defined above) from one or more algorithms are: ACOLITE (Gloria 2014-358: band 4, USC Seaprism 2016-222: bands 3 and 4), SeaDAS (GOT Seaprism 2014-026: band 4, Helsinki 2013-235: band 1, Palgrunden 2013-156: band 1, USC Seaprism 2016-222: band 4, USC Seaprism 2016-334: band 4, Venise 2015-221: band 4) and LaSRC (WaveCIS: 2013-221: bands 1 and 4). The low or negative R_{rs} retrievals from these algorithms indicate a limitation of these algorithms in dealing with the atmospheric and water quality conditions present at those match-ups.

One possible reason for the generally poor performance of ARCSI can be the aerosol contribution removal which relies on estimates from (1) dense dark vegetated surfaces, based on the assumption that reflectance of vegetated pixels is sufficiently dark, and a linear relationship between reflectance in the SWIR and blue bands or (2) dark pixels in the blue band, based on the assumption of an invariant aerosol concentration over the entire scene. However, these assumptions can easily be violated as finding a vegetated pixel that satisfies this condition may be difficult in scenes acquired over coastal waters and AOT variations may be sufficiently large such that adjoining pixels may have significantly different AOT. For the blue bands in particular, per-scene AOT estimates may lead to erroneous retrievals. For LaSRC, the generally poor performance may be due to the use of land-based pixels for aerosol estimation. In addition, for LaSRC, retrieving accurate R_{rs} estimates over water requires the presence of a considerably large land area adjoining the water pixels. The majority of the AERONET-OC sites used in this study only have relatively small nearby land surfaces. This may help explain the few instances of good performance near land masses (e.g., for the Lake Erie and Zeebrugge MOW-1 sites).

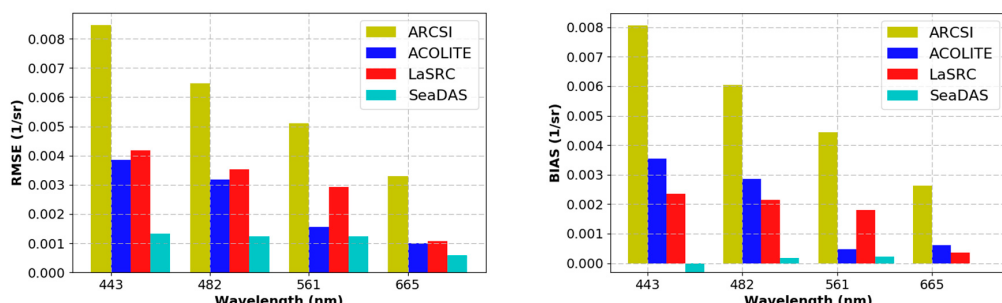


Figure 4. Overall band-by-band RMSE and mean bias results for all algorithms.

3.3. Influence of Environmental Factors for SeaDAS and ACOLITE

To understand the impact environmental factors may have on R_{rs} retrieval errors from the water-based AC methods, we investigated the influence of three variables: AOT(869), SZA, and hourly wind speed. These three variables are known to influence R_{rs} retrievals [50,51], e.g., AOT(870) and SZA have been found to reduce the quality of water-leaving radiance derived from SeaWiFS and MODIS sensors [52]. Figure 5a–c illustrates the error ($x^{\text{est}} - x^{\text{mea}}$) for each match-up point as a function of each environmental parameter, for each AC method. Negative values imply that an algorithm underestimated the observed R_{rs} value, and vice versa. We used tests of the statistical significance (two-tailed, $\alpha = 0.05$, critical value = 0.2262) of the individual Pearson correlation coefficients to guide this analysis (Pearson correlation coefficients were used to show the strength of the relationship as they have been widely used in similar studies). While ACOLITE consistently overestimated R_{rs} in the 443 and 482 nm bands, as also noted in [53], errors for both SeaDAS and ACOLITE were not significantly influenced by AOT (Figure 5a, no statistically significant correlations). However, SZA was significantly and positively correlated with R_{rs} retrieval errors from SeaDAS for all four bands (i.e., $r = 0.495486743$, 0.483529464 , 0.253699366 , and 0.427793365 , respectively), and from ACOLITE for the 443 and 482 nm bands (i.e., $r = 0.239717715$ and 0.228792001 , respectively) (Figure 5b). A similar pattern was evident for wind speed, which was significantly positively correlated with R_{rs} retrieval errors from SeaDAS for all bands except band 3 (for which a positive correlation was present, but not statistically significant) and from ACOLITE for the 443 and 482 nm bands (Figure 5c). We further examined the significance of the relationship between each environmental variable and errors across all wavelengths and found that SZA and AOT(869) were significant for SeaDAS in the first three and first two wavelengths, respectively, while ACOLITE was only influenced by wind speed in the 443 nm channel. These patterns, while generally causing only small errors in R_{rs} retrieval, may guide further developments of both AC methods to make them more robust across the range of environmental conditions.

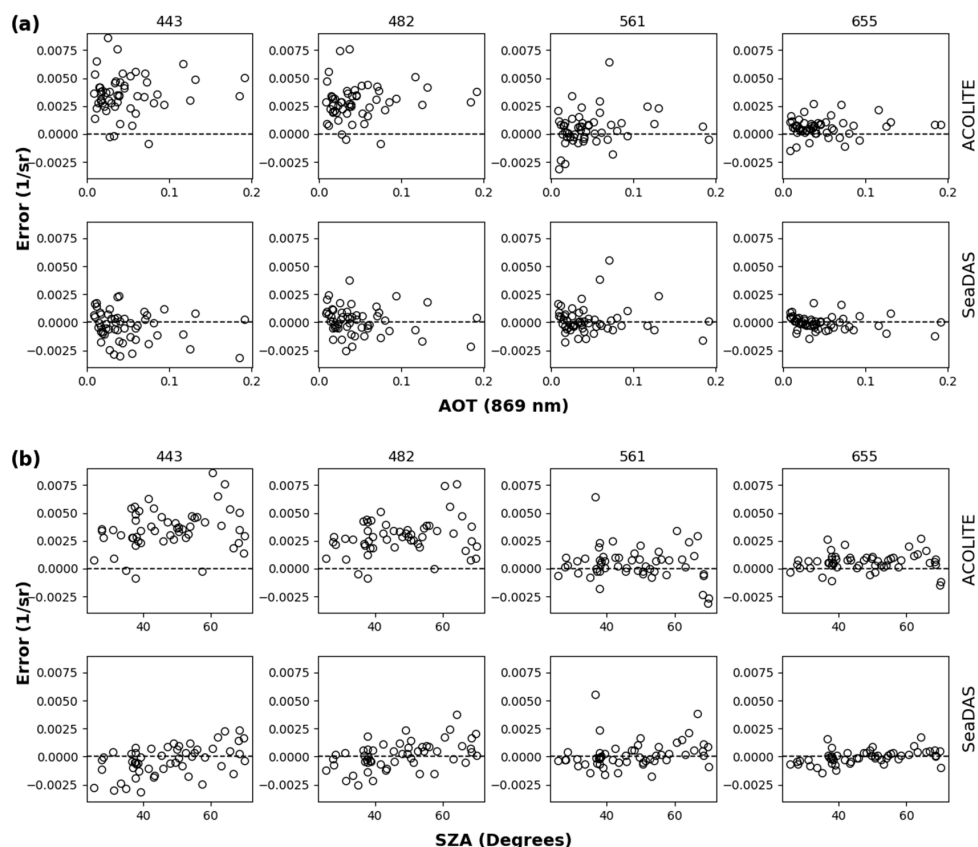


Figure 5. Cont.

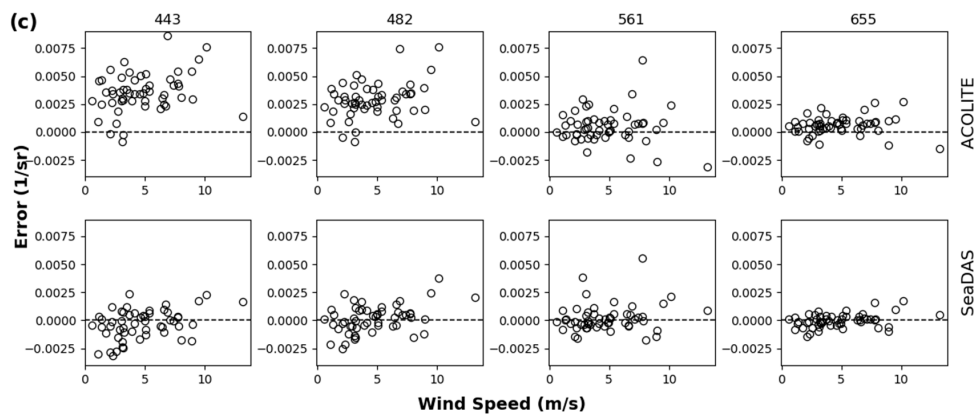


Figure 5. Scatterplots of the error (sr^{-1}) showing the dependency of R_{rs} retrieval accuracy from both ACOLITE and SeaDAS on (a) AOT(869), (b) SZA, and (c) wind speed. AOT(869) and wind speed were derived from coincident measurements at each AERONET-OC site used in this study, while SZA was obtained by subtracting the sun elevation angle provided in the Landsat 8 metadata from 90. Each circle represents a match-up data point, for a total of 54 data points across the 14 AERONET-OC sites. The 54 match-ups and their corresponding environmental parameter values are tabulated in Table A2.

4. Conclusions

This paper provides an evaluation of four atmospheric correction algorithms (ACOLITE, ARCSI, LaSRC, and SeaDAS) for estimating R_{rs} . Fifty-four match-ups were used to test the performance of these algorithms over mostly coastal sites that form part of the AERONET-OC network. After accounting for spectral band differences in AERONET-OC and OLI measurements/products, the R_{rs} products from all algorithms were compared to AERONET in-situ R_{rs} data. The generic AC methods (ARCSI and LaSRC) were less accurate for deriving R_{rs} in coastal environments than water-based methods (ACOLITE and SeaDAS). These AC methods were particularly unreliable in the 443 and 482 nm channels, and performed well at only a few sites located in nearshore and inland waters. SeaDAS produced the best performance overall, while ACOLITE, though it performed better than the two generic AC methods, was less accurate than SeaDAS for R_{rs} retrievals over (mostly) low-to-moderately coastal waters such as those typical of the AERONET-OC sites. Analyses of differences in spectral bands between satellite and in-situ measurements revealed that band adjustment minimized differences between sensors with different spectral bands. A relationship seems to exist between R_{rs} retrieval accuracy for the two water-based AC methods and two atmospheric variables: SZA and wind speed. Future studies should examine these relationships further and consider related improvements to the AC methods. Neither of the water-based AC methods can currently be used to process images from commercial sensors such as WorldView-2/3 (which have improved spatial resolution) or previous Landsat missions (though this capability is available in an in-house version of SeaDAS for future public release). Given the usefulness of high spatial resolution data and the understanding that can be gained from time-series analysis for aquatic studies, such improvements would be valuable. Our findings are primarily applicable to nearshore coastal waters under low aerosol condition (i.e., $\text{AOT}(869) \leq 0.2$). Further validation is required over inland waters (e.g., recently established sites in Green Bay, Grizzly Bay and Lake Okeechobee across the United States) and at stations with few match-up points (e.g., GOT Seaprism and Lake Erie with one and two match-ups, respectively) to better understand the performance of each AC method for various science and application areas. In future studies, the authors intend to evaluate the performance of these AC algorithms over inland waters such as those found over the GloboLakes sites.

Author Contributions: Conceptualization: C.O.I., N.P., and A.K.; Formal analysis: C.O.I., N.P., and A.K.; Investigation: C.O.I.; Methodology: C.O.I.; Project administration: N.P. and A.K.; Resources: C.O.I., N.P., and A.K.; Software: C.O.I.; Supervision: N.P. and A.K.; Validation: C.O.I.; Visualization: C.O.I.; Writing—original draft: C.O.I.; Writing—review and editing: C.O.I.

Funding: Nima Pahlevan was funded under NASA ROSES #NNX16AI16G and the USGS Landsat Science Team Award #140G0118C0011.

Acknowledgments: The authors wish to thank USGS for the distribution of Landsat 8 Level-1 data products. We are grateful for the efforts of all the staff, site support people, and the team responsible for the processing and archiving all the 14 AERONET-OC site-data used in this study. We are particularly thankful to all the principle investigators: Giuseppe Zibordi, principal investigator of the Galata Platform, Gloria, Gustav Dalen Tower, Helsinki Lighthouse, and Venise sites; Brent Holben, the principal investigator for the GOT Seaprism; Tim Moore, Steve Ruberg, and Menghua Wang, the principal investigators of the Lake Erie site; Sam Ahmed and Alex Gilerson, the principal investigators of the LISCO site, Hui Feng and Heidi M. Sosik, the principal investigators of the MVCO site; Susanne Kratzer, the principal investigator of the Palgrunden site, Dimitry Van der Zande, the principal investigator of the Thornton C-Power and Zeebrugge MOW-1 sites, Burton Jones and Curtiss Davis, the principal investigators of the USC Seaprism site, Brent Holben, the principal investigator of the USC Seaprism-2 site, and Alan Weidemann, Bill Gibson, and Robert Arnone, the principal investigators of the WaveCIS CSI-6 site. We thank Giuseppe Zibordi for answering questions about AERONET-OC data. We are deeply thankful to Quinten Vanhellemont and Kevin Ruddick for the development and support of ACOLITE, Pete Bunting and Dan Clewley for the development and support of ARCSI, the NASA Ocean Biology Processing Group for the development and support of the SeaDAS software, and the USGS Landsat Science Teams for processing the Landsat 8 to surface reflectance product (LaSRC).

Conflicts of Interest: The authors declare no conflicts of interest.

Appendix A

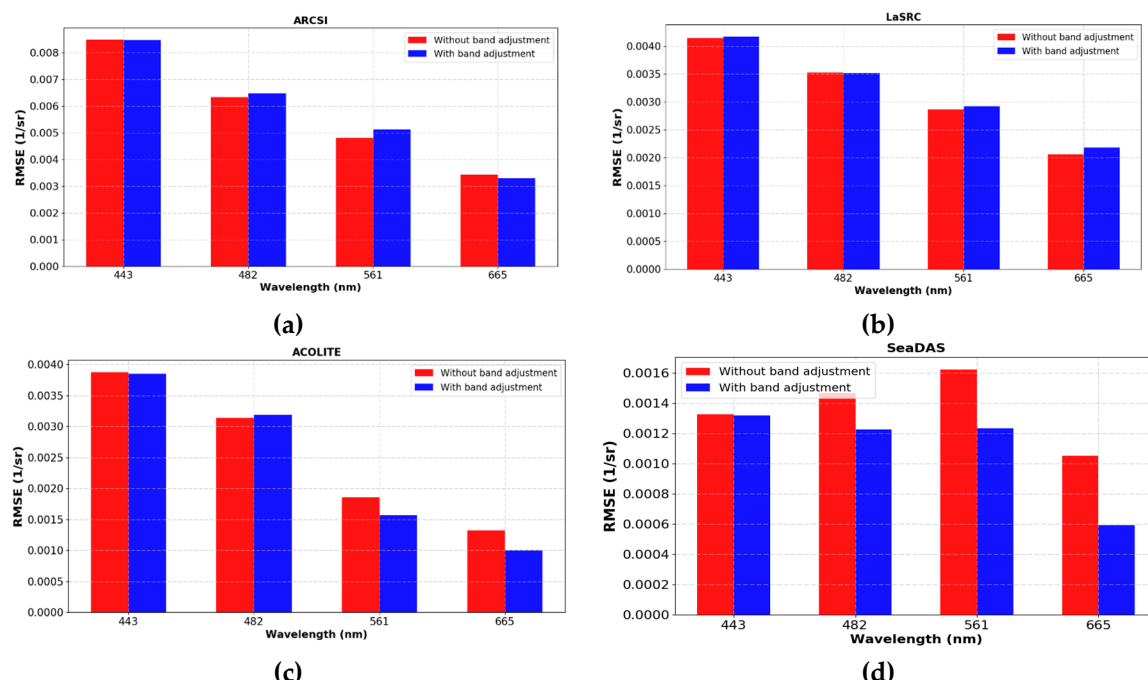


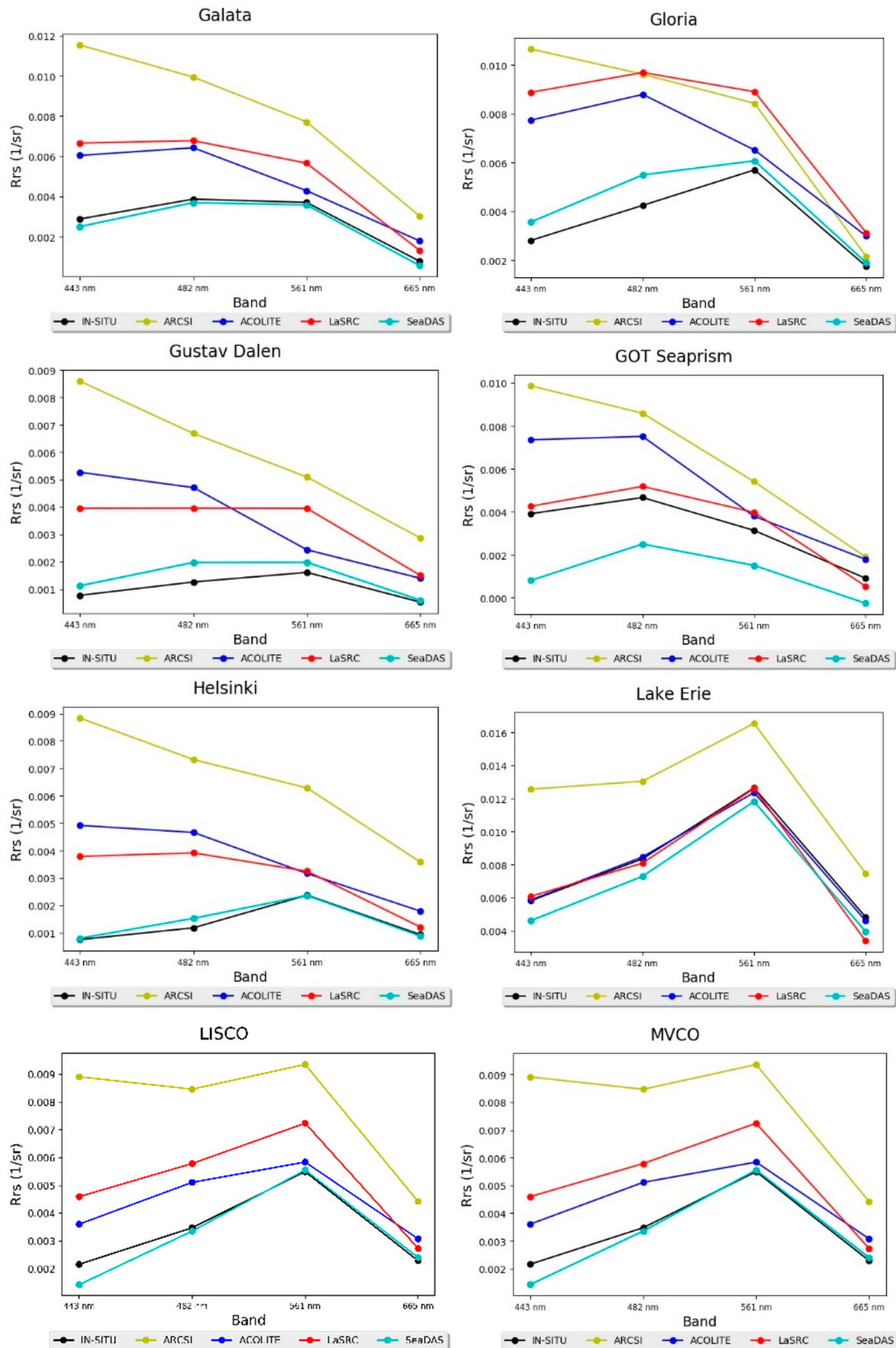
Figure A1. The root-mean-square errors showing the impacts of per-band spectral adjustment on AERONET-OC match-ups. For all AC methods, there is no noticeable effect in the 443 nm channel. Similarly, for the land-based AC methods, there are no observable differences in the 443 and 482 nm channels. Band adjustment improves the results for bands 2, 3, and 4 for SeaDAS, decreasing RMSE values by 16.6, 23.9, and 43.8% in the 482, 561, and 655 nm wavelengths, respectively, and also improves results for bands 3 and 4 for ACOLITE by 15.6 and 24.2%, respectively. For SeaDAS, the largest observable difference is in the 655 nm channel. This is by far the largest improvement from band adjustment across all bands and AC methods. Overall, SeaDAS is the most sensitive method to spectral band differences, with the largest difference (improvement) in the 655 nm channel. (a) ARCSI; (b) LaSRC; (c) ACOLITE; (d) SeaDAS.

Table A1. Satellite scenes and their correspondent sites.

Landsat Scene ID	Site
['LC81810302014141LGN00'	Galata
['LC81810302014253LGN00'	Galata
['LC81810302015240LGN00'	Galata
['LC81810302015352LGN00'	Galata
['LC81800292014086LGN00'	Gloria
['LC81800292014358LGN00'	Gloria
['LC81800292015041LGN00'	Gloria
['LC81800292015361LGN00'	Gloria
['LC81280542014026LGN00'	GOT_Seaprism
['LC81920192013151LGN00'	Gustav_Dalen_Tower
['LC81880182013235LGN00'	Helsinki_Lighthouse
['LC81880182014190LGN00'	Helsinki_Lighthouse
['LC81880182016180LGN00'	Helsinki_Lighthouse
['LC81880182016228LGN00'	Helsinki_Lighthouse
['LC81880182016260LGN00'	Helsinki_Lighthouse
['LC80200312016219LGN00'	Lake_Erie
['LC80200312016235LGN00'	Lake_Erie
['LC80130322013273LGN00'	LISCO
['LC80130322014004LGN00'	LISCO
['LC80130322015023LGN00'	LISCO
['LC80130322015279LGN00'	LISCO
['LC80130322016266LGN00'	LISCO
['LC80110312013291LGN00'	MVCO
['LC80110312014038LGN00'	MVCO
['LC80110312014150LGN00'	MVCO
['LC80110312015025LGN00'	MVCO
['LC80110312014086LGN00'	MVCO
['LC81950192013156LGN00'	Palgrunden
['LC81950192016165LGN00'	Palgrunden
['LC81990242016129LGN00'	Thornton_C-power
['LC81990242016305LGN00'	Thornton_C-power
['LC80410372014312LGN00'	USC_SEAPRISM
['LC80410372016222LGN00'	USC_SEAPRISM_2
['LC80410372016318LGN00'	USC_SEAPRISM_2
['LC80410372016334LGN00'	USC_SEAPRISM_2
['LC81920292014106LGN00'	Venise
['LC81920292015013LGN00'	Venise
['LC81920292015221LGN00'	Venise
['LC81920292016016LGN00'	Venise
['LC81920292016128LGN00'	Venise
['LC81920292016192LGN00'	Venise
['LC81920292016240LGN00'	Venise
['LC80220402013240LGN00'	WaveCIS_Site_CSI
['LC80220402013320LGN00'	WaveCIS_Site_CSI
['LC80220402014019LGN00'	WaveCIS_Site_CSI
['LC80220402014291LGN00'	WaveCIS_Site_CSI
['LC80220402014323LGN00'	WaveCIS_Site_CSI
['LC80220402015038LGN00'	WaveCIS_Site_CSI
['LC80220402015342LGN00'	WaveCIS_Site_CSI
['LC80220402016009LGN00'	WaveCIS_Site_CSI
['LC80220402016041LGN00'	WaveCIS_Site_CSI
['LC80220402016073LGN00'	WaveCIS_Site_CSI
['LC81990242014091LGN00'	Zeebrugge-MOW1
['LC81990242014219LGN00'	Zeebrugge-MOW1

Table A2. Values of environmental parameters for each match-up.

Station Date	SZA (°)	AOT 869 (nm)	Wind Speed (m/s)	Chlorophyll-a (mg/m ³)
Galata_2014141	27.68254	0.061308	4.109681	1.15
Galata_2014253	41.58995	0.116449	3.284061	1.10
Galata_2015240	37.50297	0.058537	2.129808	0.73
Galata_2015352	68.64532	0.191727	4.643727	0.62
Gloria_2014086	45.39897	0.039736	1.40709	1.03
Gloria_2014358	69.93295	0.009096	13.20025	2.28
Gloria_2015041	62.24466	0.011158	9.488579	1.64
Gloria_2015361	70.11336	0.01644	8.966497	1.31
Got_2014026	39.26405	0.184762	2.348026	0.81
Gustav_2013151	37.76921	0.045492	7.765895	1.44
Helsinki_2013235	49.6655	0.045049	7.813921	4.11
Helsinki_2014190	38.82244	0.052049	5.058227	5.19
Helsinki_2016180	38.00992	0.036343	3.183139	3.87
Helsinki_2016228	47.29317	0.015965	5.356986	3.00
Helsinki_2016260	58.31484	0.014555	7.385065	3.66
LakeErie_2016219	31.06475	0.036835	4.838009	5.32
LakeErie_2016235	35.04874	0.032271	2.098577	5.84
LISCO_2013273	45.86886	0.02143	6.629846	6.12
LISCO_2014004	65.76056	0.009206	3.691909	3.92
LISCO_2015023	63.25687	0.01911	5.097444	5.36
LISCO_2015279	48.07922	0.025828	6.469751	4.84
LISCO_2016266	43.53788	0.03848	4.592692	4.06
MVCO_2013291	53.30351	0.016554	8.056089	3.24
MVCO_2014038	60.57072	0.025061	6.897844	4.52
MVCO_2014086	43.2755	0.042702	8.934463	4.96
MVCO_2014150	25.55208	0.054678	2.590076	1.50
MVCO_2015025	64.20812	0.036832	10.15678	5.03
Palgrunden_2013156	37.03093	0.01894	3.94127	7.58
Palgrunden_2016165	36.71529	0.013707	0.5948	6.87
Thornton_2016129	36.60009	0.070453	7.756932	16.3
Thornton_2016305	66.8652	0.058625	2.756128	3.24
USCSeaPrism_2014312	52.58024	0.028872	4.974118	0.22
USCSeaPrism_2016222	37.88999	0.074677	3.123159	0.63
USCSeaPrism_2016318	54.05641	0.027335	3.450807	0.30
USCSeaPrism_2016334	57.61152	0.026866	3.217656	0.61
Venise_2014106	37.88999	0.023221	6.324373	3.41
Venise_2015013	68.62708	0.039125	3.700884	1.19
Venise_2015221	33.40939	0.125445	3.092528	0.78
Venise_2016016	68.39465	0.011226	6.740557	0.58
Venise_2016128	31.50274	0.03962	1.123216	1.01
Venise_2016192	27.88954	0.085338	1.76539	1.59
Venise_2016240	38.46594	0.033166	1.342931	1.87
WaveCIS_2013240	28.31299	0.080524	3.036319	2.15
WaveCIS_2013320	50.72926	0.069036	6.575934	2.20
WaveCIS_2014019	54.4896	0.03491	7.112117	3.99
WaveCIS_2014291	42.45005	0.016669	3.183118	1.55
WaveCIS_2014323	51.5107	0.016451	2.907233	1.53
WaveCIS_2015038	50.60994	0.022994	2.271182	1.80
WaveCIS_2015342	55.17512	0.033926	1.131623	3.37
WaveCIS_2016009	56.01941	0.072489	4.151914	3.19
WaveCIS_2016041	49.98228	0.008506	5.38026	3.97
WaveCIS_2016073	39.38958	0.052527	5.027627	2.76
Zeebruge_2014091	49.09826	0.093231	2.259445	3.42
Zeebruge_2014219	37.90776	0.13111	3.071374	4.11

**Figure A2. Cont.**

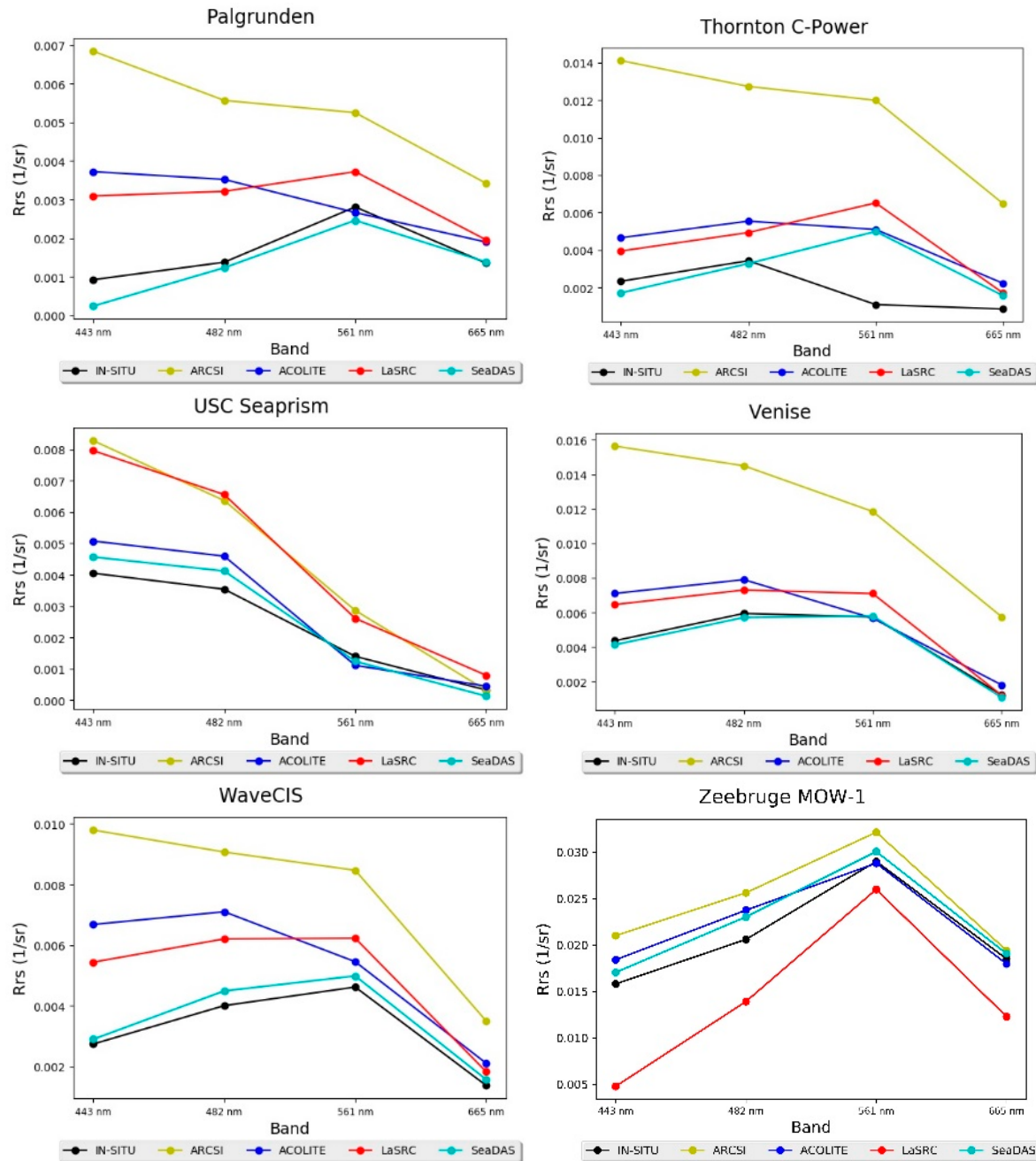


Figure A2. Line graphs showing the R_{rs} spectra of each of the 14 AERONET-OC stations (Results were averaged for each station except GOT Seaprisim for which only one match-up is available).

Table A3. Cases of negative R_{rs} retrievals from the four AC algorithms.

	ACOLITE		LaSRC		SeaDAS
561 nm	USC Seaprisim: 2016222	443 nm	WaveCIS: 2013320	443 nm	Palgrunden: 2013156
655 nm	Gloria: 2014358 USC Seaprisim: 2016222	655 nm	WaveCIS: 2013320 MVCO: 2014150	655 nm	GOT Seaprisim: 2014026 USC Seaprisim: 2016222 Venise: 2015221

References

- Cracknell, A.P.; Newcombe, S.K.; Black, A.F.; Kirby, N.E. The ABDMAP (Algal Bloom Detection, Monitoring and Prediction) Concerted Action. *Int. J. Remote Sens.* **2001**, *22*, 205–247. [CrossRef]

2. Pe'eri, S.; Parrish, C.; Azuike, C.; Alexander, L.; Armstrong, A. Satellite Remote Sensing as a Reconnaissance Tool for Assessing Nautical Chart Adequacy and Completeness. *Mar. Geod.* **2014**, *37*, 293–314. [[CrossRef](#)]
3. Dekker, A.G.; Brando, V.E.; Anstee, J.M. Retrospective Seagrass Change Detection in a Shallow Coastal Tidal Australian Lake. *Remote Sens. Environ.* **2005**, *97*, 415–433. [[CrossRef](#)]
4. Mumby, P.J.; Green, E.P.; Edwards, A.J.; Clark, C.D. Coral Reef Habitat Mapping: How Much Detail Can Remote Sensing Provide? *Mar. Biol.* **1997**, *130*, 193–202. [[CrossRef](#)]
5. Gordon, H.R.; Wang, M. Retrieval of Water-Leaving Radiance and Aerosol Optical Thickness over the Oceans with SeaWiFS: A Preliminary Algorithm. *Appl. Opt.* **1994**, *33*, 443. [[CrossRef](#)] [[PubMed](#)]
6. Antoine, D.; Morel, A. A Multiple Scattering Algorithm for Atmospheric Correction of Remotely Sensed Ocean Colour (MERIS Instrument): Principle and Implementation for Atmospheres Carrying Various Aerosols Including Absorbing Ones. *Int. J. Remote Sens.* **1999**, *20*, 1875–1916. [[CrossRef](#)]
7. Mobley, C.D.; Werdell, J.; Franz, B.; Ahmad, Z.; Bailey, S. Atmospheric Correction for Satellite Ocean Colour Radiometry. Available online: <https://oceancolor.gsfc.nasa.gov/docs/technical/NASA-TM-2016-217551.pdf> (accessed on 18 February 2019).
8. IOCCG. *Remote Sensing of Ocean. Colour in Coastal, and Other Optically-Complex. Waters*; Sathyendranath, S., Ed.; Reports of the International Ocean-Colour Coordinating Group (IOCCG); IOCCG: Dartmouth, NS, Canada, 2000.
9. Siegel, D.A.; Wang, M.; Maritorena, S.; Robinson, W. Atmospheric Correction of Satellite Ocean Colour Imagery: The Black Pixel Assumption. *Appl. Opt.* **2000**, *39*, 3582–3591. [[CrossRef](#)] [[PubMed](#)]
10. Shi, W.; Wang, M. An Assessment of the Black Ocean Pixel Assumption for MODIS SWIR Bands. *Remote Sens. Environ.* **2009**, *113*, 1587–1597. [[CrossRef](#)]
11. Wang, M.; Shi, W. The NIR-SWIR Combined Atmospheric Correction Approach for MODIS Ocean Colour Data Processing. *Opt. Exp.* **2007**, *15*, 15722–15733. [[CrossRef](#)]
12. Bailey, S.W.; Franz, B.A.; Werdell, P.J. Estimation of Near-Infrared Water-Leaving Reflectance for Satellite Ocean Colour Data Processing. *Opt. Exp.* **2010**, *18*, 7521–7527. [[CrossRef](#)] [[PubMed](#)]
13. Goyens, C.; Jamet, C.; Schroeder, T. Evaluation of Four Atmospheric Correction Algorithms for MODIS-Aqua Images over Contrasted Coastal Waters. *Remote Sens. Environ.* **2013**, *131*, 63–75. [[CrossRef](#)]
14. Jamet, C.; Loisel, H.; Kuchinke, C.P.; Ruddick, K.; Zibordi, G.; Feng, H. Comparison of three SeaWiFS atmospheric correction algorithms for turbid waters using AERONET-OC measurements. *Remote Sens. Environ.* **2011**, *115*, 1955–1965. [[CrossRef](#)]
15. Pahlevan, N.; Schott, J.R.; Franz, B.A.; Zibordi, G.; Markham, B.; Bailey, S.; Schaaf, C.B.; Ondrusek, M.; Gren, S.; Strait, C.M. Landsat 8 remote sensing reflectance (Rrs) products: Evaluations, intercomparisons, and enhancements. *Remote Sens. Environ.* **2017**, *190*, 289–301. [[CrossRef](#)]
16. Pahlevan, N.; Lee, Z.; Wei, J.; Schaaf, C.B.; Schott, J.R.; Berk, A. On-orbit radiometric characterization of OLI (Landsat-8) for applications in aquatic remote sensing. *Remote Sens. Environ.* **2014**, *154*, 272–284. [[CrossRef](#)]
17. Hedley, J.; Roelfsema, C.; Koetz, B.; Phinn, S. Capability of the Sentinel 2 Mission for Tropical Coral Reef Mapping and Coral Bleaching Detection. *Remote Sens. Environ.* **2012**, *120*, 145–155. [[CrossRef](#)]
18. Franz, B.A.; Bailey, S.; Kuring, N.; Werdell, P.J. Ocean Colour Measurements with the Operational Land Imager on Landsat-8: Implementation and Evaluation in SeaDAS. *J. Appl. Remote Sens.* **2015**, *9*, 096070. [[CrossRef](#)]
19. Doxani, G.; Vermote, E.; Roger, J.; Gascon, F.; Adriaensen, S.; Frantz, D.; Hagolle, O.; Hollstein, A.; Kirches, G. Atmospheric Correction Inter-Comparison Exercise. *Remote Sens.* **2018**, *10*, 352. [[CrossRef](#)]
20. Wei, J.; Lee, Z.; Garcia, R.; Zoffoli, L.; Armstrong, R.A.; Shang, Z.; Sheldon, P.; Chen, R.F. An assessment of Landsat-8 atmospheric correction schemes and remote sensing reflectance products in coral reefs and coastal turbid waters. *Remote Sens. Environ.* **2018**, *215*, 18–32. [[CrossRef](#)]
21. Clewley, D.; Bunting, P.; Shepherd, J.; Gillingham, S.; Flood, N.; Dymond, J.; Lucas, R.; Armston, J.; Moghaddam, M. A Python-Based Open Source System for Geographic Object-Based Image Analysis (GEOBIA) Utilizing Raster Attribute Tables. *Remote Sens.* **2014**, *6*, 6111–6135. [[CrossRef](#)]
22. Vanhellemont, Q.; Ruddick, K. Turbid Wakes Associated with Offshore Wind Turbines Observed with Landsat 8. *Remote Sens. Environ.* **2014**, *145*, 105–115. [[CrossRef](#)]
23. USGS. Product Guide: Landsat 8 Surface Reflectance Code (LASRC) Product, 2017. Available online: <https://doi.org/10.1080/1073161X.1994.10467258> (accessed on 18 February 2019).

24. Vermote, E.F.; Justice, C.; Claverie, M.; Franch, B. Preliminary Analysis of the Performance of the Landsat 8/OLI Land Surface Reflectance Product. *Remote Sens. Environ.* **2016**. [[CrossRef](#)]
25. Gerace, A.D.; Schott, J.R.; Nevins, R. Increased Potential to Monitor Water Quality in the Near-Shore Environment with Landsat's next-Generation Satellite. *J. Appl. Remote Sens.* **2013**, *7*, 073558. [[CrossRef](#)]
26. Zibordi, G.; Holben, B.; Slutsker, I.; Giles, D.; D'Alimonte, D.; Mélin, H.; Berthon, J.F. AERONET-OC: A Network for the Validation of Ocean Colour Primary Products. *J. Atmos. Ocean. Tech.* **2009**, *26*, 1634–1651. [[CrossRef](#)]
27. Holben, B.N.; Tanré, D.; Smirnov, A.; Eck, T.F.; Slutsker, I.; Abu Hassan, N.; Newcomb, W.W.; Schafer, J.S.; Chatenet, B.; Lavenu, F. An Emerging Ground-Based Aerosol Climatology: Aerosol Optical Depth from AERONET. *J. Geophys. Res.* **2001**, *106*, 12067. [[CrossRef](#)]
28. Holben, B.N.; Eck, T.F.; Slutsker, I.; Tanré, D.; Buis, J.P.; Setzer, A.; Vermote, E.; Reagan, J.A.; Kaufman, T.; Nakajima, F. AERONET-A Federated Instrument Network and Data Archive for Aerosol Characterization. *Remote Sens. Environ.* **1998**, *66*, 1–16. [[CrossRef](#)]
29. Thuillier, G.; Hersé, M.; Simon, P.C.; Labs, D.; Mandel, H.; Gillotay, D.; Foujols, T. The Solar Spectral Irradiance from 200 to 2400 nm as Measured by the SOLSPEC Spectrometer from the ATLAS and EURECA Missions. *Sol. Phys.* **2003**, *214*, 1–22. [[CrossRef](#)]
30. Bailey, S.; Franz, A.; Werdell, J. A Multi-Sensor Approach for the on-Orbit Validation of Ocean Colour Satellite Data Products. *Remote Sens. Environ.* **2006**, *102*, 12–23. [[CrossRef](#)]
31. Wicks, D.J.; Jarman, M. S2 ARD Project Briefing Document. 2017. Available online: https://media.sa.catapult.org.uk/wp-content/uploads/2017/09/14123619/Sentinel-2-ARD-Project-Summary_final.pdf (accessed on 22 February 2018).
32. Wilson, R.T. Py6S: A Python Interface to the 6S Radiative Transfer Model. *Comput. Geosci.* **2013**, *51*, 166–171. [[CrossRef](#)]
33. Vermote, E.F.; Tanré, D.; Deuzé, J.L.; Herman, M.; Morcrette, J.J. Second Simulation of the Satellite Signal in the Solar Spectrum, 6S: An Overview. *IEEE Trans. Geosci. Remote Sens.* **1997**, *35*, 675–686. [[CrossRef](#)]
34. Vanhellemont, Q.; Ruddick, K. Landsat-8 As a Precursor to Sentinel-2: Observations of Human Impacts in Coastal Waters. In Proceedings of the Sentinel-2 for Science Workshop, Frascati, Italy, 20–23 May 2014.
35. Shettle, E.P.; Fenn, R.W. Models for the Aerosols of the Lower Atmosphere and the Effects of Humidity Variations on Their Optical Properties. *Environ. Res.* **1979**, *676*. [[CrossRef](#)]
36. Ruddick, K.G.; Ovidio, F.; Rijkeboer, M. Atmospheric Correction of SeaWiFS Imagery for Turbid Coastal and Inland Waters. *Appl. Opt.* **2000**, *39*, 897–912. [[CrossRef](#)]
37. Vanhellemont, Q.; Ruddick, K. Acolite for sentinel-2: Aquatic applications of MSI imagery. In Proceedings of the 2016 ESA Living Planet Symposium, Prague, Czech Republic, 9–13 May 2016.
38. Wang, Y.; Liu, L.; Hu, Y.; Li, D.; Li, Z.; Wang, Y. Development and Validation of the Landsat-8 Surface Reflectance Products Using a MODIS-Based per-Pixel Atmospheric Correction Method Atmospheric Correction Method. *Int. J. Remote Sens.* **2016**, *37*, 1291–1314. [[CrossRef](#)]
39. Wang, Z.; Erb, A.M.; Schaaf, C.B.; Sun, Q.; Liu, Y.; Yang, Y.; Shuai, Y.; Casey, K.A.; Román, M.O. Early Spring Post-Fire Snow Albedo Dynamics in High Latitude Boreal Forests Using Landsat-8 OLI Data. *Remote Sens. Environ.* **2015**, *185*, 71–83. [[CrossRef](#)] [[PubMed](#)]
40. Vuolo, F.; Mattiuzzi, M.; Atzberger, C. Comparison of the Landsat Surface Reflectance Climate Data Record (CDR) and Manually Atmospherically Corrected Data in a Semi-Arid European Study Area. *Int. J. Appl. Earth Obs. Geoinf.* **2015**, *42*, 1–10. [[CrossRef](#)]
41. Feng, M.; Sexton, J.O.; Huang, C.; Masek, J.G.; Vermote, E.F.; Gao, F.; Narasimhan, R.; Channan, S.; Wolfe, R.E.; Townshend, J.R. Global Surface Reflectance Products from Landsat: Assessment Using Coincident MODIS Observations. *Remote Sens. Environ.* **2013**, *134*, 276–293. [[CrossRef](#)]
42. Ahmad, Z.; Franz, B.; McClain, C.; Kwiatkowska, E.; Werdell, J.; Shettle, E.; Holben, B. New Aerosol Models for the Retrieval of Aerosol Optical Thickness and Normalized Water-Leaving Radiances from the SeaWiFS and MODIS Sensors over Coastal Regions and Open Oceans. *Appl. Opt.* **2010**, *49*, 5545–5556. [[CrossRef](#)] [[PubMed](#)]
43. Gordon, H.R.; Wang, M. Influence of Oceanic Whitecaps on Atmospheric Correction of Ocean-Colour Sensors. *Appl. Opt.* **1994**, *33*, 7754. [[CrossRef](#)] [[PubMed](#)]
44. Pahlevan, N.; Smith, B.; Binding, C.; O'Donnell, D.M. Spectral Band Adjustments for Remote Sensing Reflectance Spectra in Coastal/Inland Waters. *Opt. Exp.* **2017**, *25*, 28650–28667. [[CrossRef](#)]

45. Mélin, F.; Sclep, G. Band Shifting for Ocean Colour Multi-Spectral Reflectance Data. *Opt. Exp.* **2015**, *23*, 2262–2279. [[CrossRef](#)] [[PubMed](#)]
46. Pahlevan, N.; Roger, J.; Ahmad, Z. Revisiting short-wave-infrared (SWIR) bands for atmospheric correction in coastal waters. *Opt. Exp.* **2107**, *25*, 6015–6035. [[CrossRef](#)] [[PubMed](#)]
47. Vanhellemont, Q.; Ruddick, K. Advantages of high quality SWIR bands for ocean colour processing: Examples from Landsat-8. *Remote Sens. Environ.* **2015**, *161*, 89–106. [[CrossRef](#)]
48. De Maerschalck, B.; Vanlede, J. Zeebrugge Harbour Sediment Transport Model. *Coast. Dyn.* **2013**, *477–486*.
49. Amin, R.; Gilerson, A.; Zhou, J.; Gross, B.; Moshary, F.; Ahmed, S. Impacts of Atmospheric Corrections on Algal Bloom Detection Techniques. In Proceedings of the Eighth Conference on Coastal Atmospheric, Oceanic Prediction, Phoenix, AZ, USA, 11–15 January 2009.
50. Mobley, C.D. Estimation of the Remote-Sensing Reflectance from above-Surface Measurements. *Appl. Opt.* **1999**, *38*, 7442. [[CrossRef](#)] [[PubMed](#)]
51. Kaufman, Y.J. Aerosol Optical Thickness and Atmospheric Path Radiance. *J. Geophys. Res.* **1993**, *98*, 2677–2692. [[CrossRef](#)]
52. Zibordi, G.; Mélin, F.; Berthon, J.F. Comparison of SeaWiFS, MODIS and MERIS radiometric products at a coastal site. *Geophys. Res. Lett.* **2006**, *33*, 1–4. [[CrossRef](#)]
53. Vanhellemont, Q.; Bailey, S.; Franz, B.; Shea, D. Atmospheric Correction of Landsat-8 Imagery Using Seadas. In Proceedings of the Sentinel-2 for Science Workshop, Frascati, Italy, 20–23 May 2014.



© 2019 by the authors. Licensee MDPI, Basel, Switzerland. This article is an open access article distributed under the terms and conditions of the Creative Commons Attribution (CC BY) license (<http://creativecommons.org/licenses/by/4.0/>).